Nonresonant and Resonant Frequency-Selectable Induction-Heating Targets

John I. Rodriguez, *Member, IEEE*, and Steven B. Leeb, *Fellow, IEEE*

***Abstract*—This paper examines a scheme for developing frequency-selectable induction-heating targets for stimulating temperature-sensitive polymer gels. The phrase "frequency selectable" implies that each target has a frequency at which it heats preferentially in the presence of other targets. Targets using both nonresonant and resonant designs are discussed. In the case of nonresonant targets, single-turn conductors whose critical dimensions are small compared to their associated skin depth (over the frequency range of interest) are examined. One way to achieve frequency selectivity with these nonresonant targets is by designing each to have the same self-inductance while forcing the resistance of each target to differ from the previous one by a specified factor (α). In this way, a target driven at its R/L break-point frequency will heat by at least a factor of $(\alpha^2 + 1)/(2\alpha)$ more than the remaining targets. In the resonant-target case, RLC circuits that are inductively coupled to a primary induction coil are examined. Frequency selectivity in resonant targets is achieved by designing each target to have a different resonant frequency. When such a target is driven at its resonant frequency, it will heat preferentially compared to the remaining targets.**

***Index Terms*—Induction heating, Marx inverter, RL circuits, RLC circuits.**

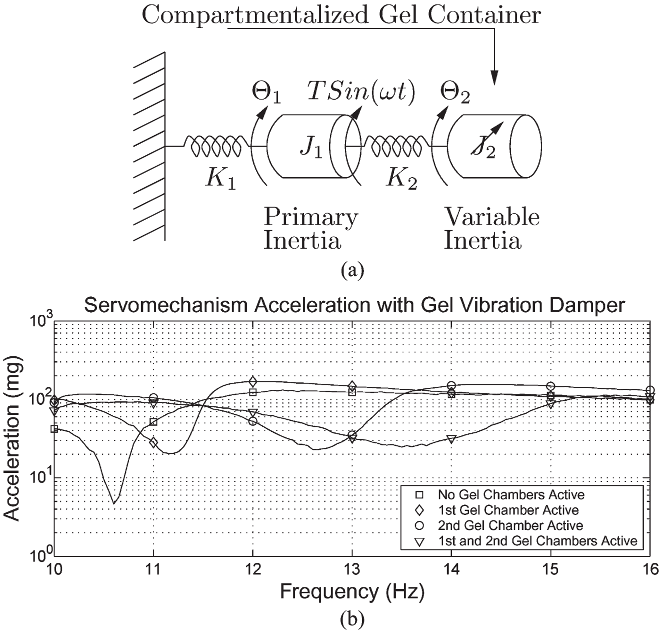

Fig. 1. Torsional gel damper. (a) Simplified model. (b) Acceleration response versus frequency of the primary inertia J_1.

I. BACKGROUND

AN ADAPTIVE vibration damper that is capable of adjusting its natural frequency to improve damping over a range of vibration frequencies was developed. This damper is an auxiliary spring–mass system and is sometimes referred to as a dynamic vibration absorber (DVA) [1]. When a DVA is mechanically coupled to a vibrating structure, such as an automobile engine, or a building, it creates a higher order mechanical system with at least one resonance and one antiresonance. At the DVA's natural frequency, the total system experiences an antiresonance where the mass of the DVA and the mass of the vibrating structure move in counterpoise. The mass of the primary mechanical structure remains relatively stationary, while the DVA oscillates as a result of "absorbing" the disturbing vibration.

Typically, a DVA is designed to provide maximum damping at its fixed natural frequency. A more sophisticated DVA can adjust its natural frequency by varying its spring constant with a magnetic actuator, a responsive material, or some other scheme [2]. Because the DVA concept applies equally well to both linear and rotational systems, a controllable moment of inertia can also be exploited. Fig. 1(a) shows a simplified model of a rotational DVA with an adjustable moment of inertia. A variable inertia (J_2) is created using a cylindrical container filled with a gel fluid. This fluid consists of temperature-sensitive polymer gel beads suspended in a solvent [3]. Below a certain temperature, the gel beads swell, absorbing the surrounding solvent into the polymer matrix (like a sponge). When this happens, the gel beads pack tightly in the container, adding significantly to the container's effective moment of inertia. At higher temperatures, the polymer network shrinks, allowing the solvent to flow freely. This effectively decouples the gel–solvent mass and lowers the apparent rotational inertia J_2. By subdividing the container into n compartments of varying gel mass, 2^n antiresonant states are made possible, depending on which compartments are heated. Fig. 1(b) shows peak damping at four different vibration frequencies created by a two-compartment gel DVA prototype.

II. GEL INDUCTION-HEATING SYSTEM

By design, each gel compartment must be hermetically sealed and allowed to oscillate mechanically with as little

---

Manuscript received April 13, 2009; revised September 5, 2009; accepted October 20, 2009. Date of publication December 15, 2009; date of current version August 11, 2010. This work was supported in part by the National Science Foundation through a Materials Research Science and Engineering Center grant to Massachusetts Institute of Technology's Center for Materials Science and Engineering, in part by the Grainger Foundation through a grant, and in part by Ford Motor Company.

J. I. Rodriguez was with NEMOmetrics Corporation, Brighton, MA 02135 USA (e-mail: johnrodriguez@alum.mit.edu).

S. B. Leeb is with the Department of Electrical Engineering and Computer Science and the Department of Mechanical Engineering, Massachusetts Institute of Technology, Cambridge, MA 02139 USA.

Digital Object Identifier 10.1109/TIE.2009.2037676

external damping as possible. Heating schemes that need to make contact with a gel compartment are therefore undesirable. One potential solution to this problem is induction heating. Traditionally, induction heating has been used for applications that include cooking [4], as well as various industrial processes such as melting, annealing, and hardening [5]. However, in the past, induction heating was also successfully used to trigger single gel polymers without physical contact [6]. While ongoing research in the area of induction heating ranges from coil design [7] and load modeling [8] to control algorithms [9], the majority of these applications deal with single loads. Because the gel-based DVA has multiple compartments, an induction-heating system that can selectively heat any combination of loads (compartments) is desired.

There are a variety of ways through which selective compartment heating can be achieved. One basic approach would be to use separate induction coils and drive circuits for each compartment. For instance, [10] proposes some interesting topologies for dealing with the problem of multiple burners (multicoils) for induction cooking. In the gel induction-heating system, this approach is not without some limitations as it must address the effect of mutual coupling between coils. Recently, [11] demonstrated a zone-controlled induction-heating system that actively corrects for the effects of mutual coupling, but their work is focused primarily on providing uniform heating in all zones simultaneously and not selectively. Furthermore, these multiple drive/load approaches are hardware intensive. Others have suggested less component intensive solutions by reducing the number of drives. Some examples include a dual-load induction-heating topology [12] and a single-inverter multiload induction-heating system [13]. Unfortunately, all of these approaches require multiple primary-side induction-heating coils. Another intriguing idea patented by [14] proposes that a single coil could provide controllable zones if the coil is tapped at appropriate locations with separate capacitors to create zones that respond to unique resonant frequencies. This patent also introduces the notion that a single power supply that is capable of driving a sum of sine waves across a single induction coil could be used to heat the desired combination of inductively coupled targets, although no actual drive topology is given. While this zoned induction-heating approach has some merit, it would constrain the gel DVA's design to axially aligned compartments.

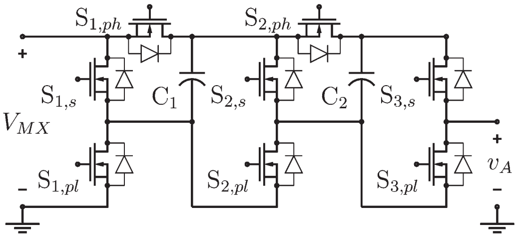

Fig. 2. Single-phase four-level Marx inverter.

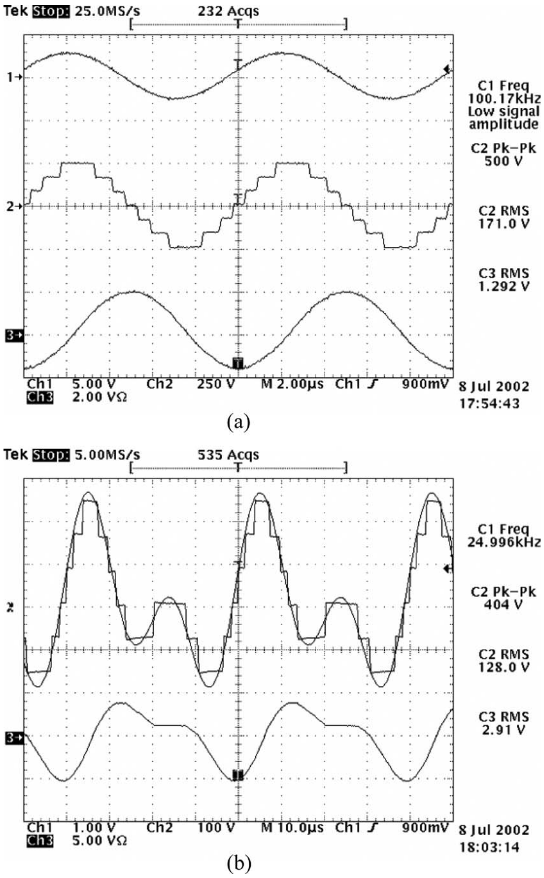

Fig. 3. Sample Marx inverter waveforms. Channels 1, 2, and 3 are the reference waveform, Marx output voltage, and load current, respectively. For scaling purposes, the measurements on channel 3 are consistent with $1\ \text{V} \cdot \Omega = 1\ \text{A}$. Two different reference waveform and load configurations are shown: (a) 100-kHz sine wave, 200-μH air core inductor and (b) sum of sine waves (25 kHz, 50 kHz), 200-μH air core inductor.

The approach taken in this paper is less restrictive of potential compartment geometries. This freedom is achieved by outfitting each gel compartment with an induction target that has been designed to heat preferentially at one frequency (with respect to the other targets) and using only a single primary-side induction coil to couple to them. This configuration requires a single power supply that is capable of providing power at multiple frequencies. Possible power supplies that could do this include linear power amplifiers and pulsewidth-modulated inverters. Another possibility would include certain multilevel inverters (for more information on multilevel inverters, the reader is referred to [15] and [16], both which contain excellent reviews on the subject). Unfortunately, most multilevel inverter topologies are unsuitable for induction heating because of a well-known capacitor voltage imbalance that occurs during real power delivery; addressing this imbalance is an area of ongoing research [17]. The cascaded multilevel inverters with separate voltage sources [18] are examples of a suitable topology for this application, but it requires multiple voltage sources. Another possibility, the one explored in this paper, is to approximate the desired sum of sine waves using the recently developed Marx inverter. This multilevel inverter is capable of simultaneously delivering real power at multiple frequencies and is the subject of a separate paper [19]. For illustration, one phase leg of a four-level Marx inverter is shown in Fig. 2. By using two of these phase legs, an induction coil can be driven differentially to generate the necessary waveforms. Some sample waveforms are shown in Fig. 3. Each scope plot shows three waveforms that correspond (from top to bottom) to the desired reference waveform, the multilevel approximation, and the current drawn from the converter when driving an induction-heating coil. The reader is referred to [19] for a detailed discussion of this inverter and its operation. The remainder of this paper focuses on the design of frequency-selectable targets suitable for the previously described gel induction-heating system. For the purposes of discussion, the frequency-selectable induction targets that have been developed here can be broadly divided into two classes: nonresonant and resonant targets. Each class offers its own advantages and disadvantages and will be discussed in turn. The first class, namely, nonresonant targets, can be modeled as individual RL circuits that are each coupled to a primary induction coil. These targets achieve selective heating by varying the resistance of each target [20]. Similarly, the resonant targets discussed here are the ones that can be modeled as RLC circuits that are likewise inductively coupled to a primary heating coil. In the resonant case, the target's capacitance is chosen so that the effective series resistance in the circuit dissipates power preferentially at the circuit's resonant frequency [21]. Since the initial work on both [20] and [21], their respective design equations have been standardized in order to better show the relationship between both types of targets. By presenting both classes of target together, a designer can gain a better understanding of which type of target to choose for an application. The designer can also choose to drive the primary coil with either a voltage or current source, and the implications of both source types are discussed.

III. NONRESONANT FREQUENCY-SELECTABLE INDUCTION-HEATING TARGETS

This section describes nonresonant frequency-selectable targets that can be described as inductively coupled RL circuits. By varying each target's resistance, selective heating can be achieved without the need for a resonant capacitor. "Thin-walled" conductors are prime candidates for use as induction targets in the DVA. The term "thin walled" has two meanings. First, it implies that the volume consumed by the target is negligible compared to the gel volume that it is heating. Second, it also implies that the conductor thickness is small compared to its skin depth at the frequencies of interest. This criterion leads to a simple circuit model description for each target. To understand why this is the case, it is helpful to understand induction heating in the context of thin-walled conductors.

The term "induction heating" refers to situations where a time-varying magnetic field gives rise to eddy currents in a conductor and, therefore, ohmic dissipation. In a typical case, these eddy currents crowd near the conductor's surface with a profile that decays exponentially into the conductor at a rate determined by its skin depth δ. These eddy currents terminate the time-varying magnetic field, permitting the conductor to act as a shield. If additional shielding or heating is needed, the conductor's thickness can be increased until the magnetic field is completely terminated. Perhaps counterintuitively, a thin-walled conductor whose thickness is small compared to its skin depth δ can also act as a good magnetic shield or induction target. This phenomenon is explained in [23] and summarized with the help of Fig. 4.

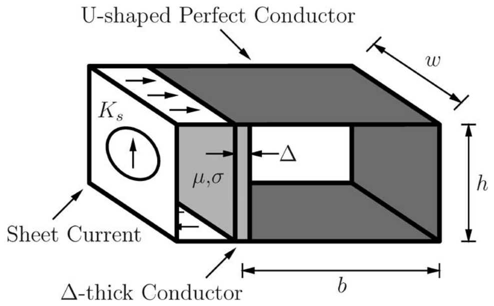

Fig. 4. Perfectly conducting U-shaped conductor that is bridged by a Δ-thick conductor and driven by a sinusoidal current sheet can be used to illustrate how a thin-walled conductor can act as a magnetic shield or induction-heating target.

Here, a perfectly conducting U-shaped conductor is driven by a sheet current $K_s = K_o \sin(\omega t)$, where it is assumed that the conductor's width w is great enough to eliminate variation of the field solution along this axis. A Δ-thick conductor bridges the open end of the U-shaped conductor. When the Δ-thick conductor is such that $\Delta \ll \delta$, it can be thought of as forming a current divider with the U-shaped perfect conductor. If the conductance per unit width is defined as $G = \sigma\Delta/h$ and the inductance times a unit width is determined as $L = \mu bh$, for this structure, the complex amplitude of the current flowing through the Δ-thick conductor can be expressed as

$$K_\Delta = \frac{j\omega LG}{1 + j\omega LG} K_o. \tag{1}$$

Essentially, the magnetic energy stored in the region to the right of the Δ-thick conductor in Fig. 4 is modeled as energy stored in a lumped inductor. As the drive frequency increases, the effective impedance of this inductance increases also, forcing a greater fraction of the drive current into the resistive sheet. This frequency response is analogous to the current that flows through the resistive leg of a parallel RL circuit when driven by a sinusoidal current-source input. Consequently, the Δ-thick conductor can be modeled as a parallel RL circuit, provided that $\Delta \ll \delta$ over the frequencies of interest. Unlike the thick-conductor case, the shielding (or heating) strategy for the thin conductor is to increase the length (b) of the U-shaped conductor, thereby increasing its inductance and shunting more current through the Δ-thick conductor for a given frequency. Provided that the RL circuit is a good model, a frequency-selectable heating scheme can be devised if a collection of targets are designed to have similar self-inductances (L_n) but different resistances (R_n). The most straightforward way to achieve this is to use similar geometries for each target to match their self-inductances while using metals with different conductivities or thicknesses to specify the desired resistances. An example is shown in Fig. 5. Three shorted wires or sheets of different alloys form single-turn inductors with different resistances. All three are coupled to a single primary induction coil, with inductance (L_0) and resistance (R_0). The primary coil used to excite these targets can be driven with either a current or a voltage source. Because the current-drive case is easier to analyze, it will be discussed first.

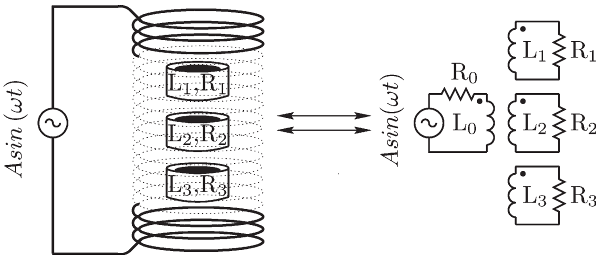

Fig. 5. Induction-heating circuit for three different targets. Amplitude (A) can be current (I_o) or voltage (V_o), depending on the drive type.

A. Induction Heating: Current-Drive Case

If the primary coil is driven by a sinusoidal current with amplitude I_o and the cross-coupling between induction targets is negligible, the power delivered to a target is independent of the power delivered to any remaining target. In this case, the time-averaged power dissipated in a target n can be expressed as

$$\langle P_n(\omega)\rangle = \frac{(I_o K_n \omega)^2 L_0 L_n R_n}{2\left[(L_n\omega)^2 + R_n^2\right]}. \tag{2}$$

The term K_n represents the coupling coefficient between the primary coil and target n and is defined using the mutual inductance (L_{0n}) between L_0 and L_n

$$K_n = \frac{L_{0n}}{\sqrt{L_0 L_n}}. \tag{3}$$

If target n (one, two, or three) is driven at its -3-dB break-point frequency in hertz

$$f_n = \frac{\omega_n}{2\pi} = \frac{R_n}{2\pi L_n} \tag{4}$$

the equation for time-averaged power reduces to the following:

$$\langle P_n(f_n)\rangle = \frac{\pi}{2} L_0 (K_n \cdot I_o)^2 f_n. \tag{5}$$

It is interesting to note from this equation that at the break-point frequency of the target, the only way to increase power dissipation is by increasing the current or inductance on the primary side or by improving the coupling between the coil and the target. The absolute values of the target's self-inductance or resistance are irrelevant because only their ratio matters. If the targets are further constrained so that the resistance between one target and the next differs by a factor of α, i.e., $R_{n+1} = \alpha R_n$, it can be shown that the time-averaged power dissipated in R_n when driven at its break-point frequency with respect to the closest higher frequency target is

$$\langle P_n(f_n)\rangle = \frac{\alpha^2+1}{2\alpha}\left(\frac{K_n}{K_{n+1}}\right)^2 \langle P_{n+1}(f_n)\rangle. \tag{6}$$

Similarly, the time-averaged power dissipated in R_n with respect to the closest lower frequency target is

$$\langle P_n(f_n)\rangle = \frac{\alpha^2+1}{2\alpha}\left(\frac{K_n}{K_{n-1}}\right)^2 \langle P_{n-1}(f_n)\rangle. \tag{7}$$

These results are more readily appreciated by plotting the power profiles for three hypothetical targets versus frequency, as shown in Fig. 6(a). The coupling coefficient of all targets has been chosen to be equal to 0.3, and the three targets have break-point frequencies that are separated by factors of five, specifically 4, 20, and 100 kHz. Under these constraints, each target experiences preferential heating with respect to the remaining targets over some frequency range. The extent of preferential heating is given as a ratio in Fig. 6(b) for this example. Because of the identical coupling and the even spacing in break-point frequencies, each target experiences power dissipation of at least 2.6 times more than any of the remaining targets when driven at its break-point frequency—as suggested by (6) and (7). From these equations, it is apparent that the degree of achievable preferential heating is modest. While this may limit the number of applications for nonresonant targets, it is more than sufficient for selectively stimulating gel polymers. From (5), it is apparent that a fixed current results in higher power dissipation at higher frequencies. In order to equalize the absolute power delivered to all targets, the amplitude of the current driving the primary coil can be controlled via the following relationship:

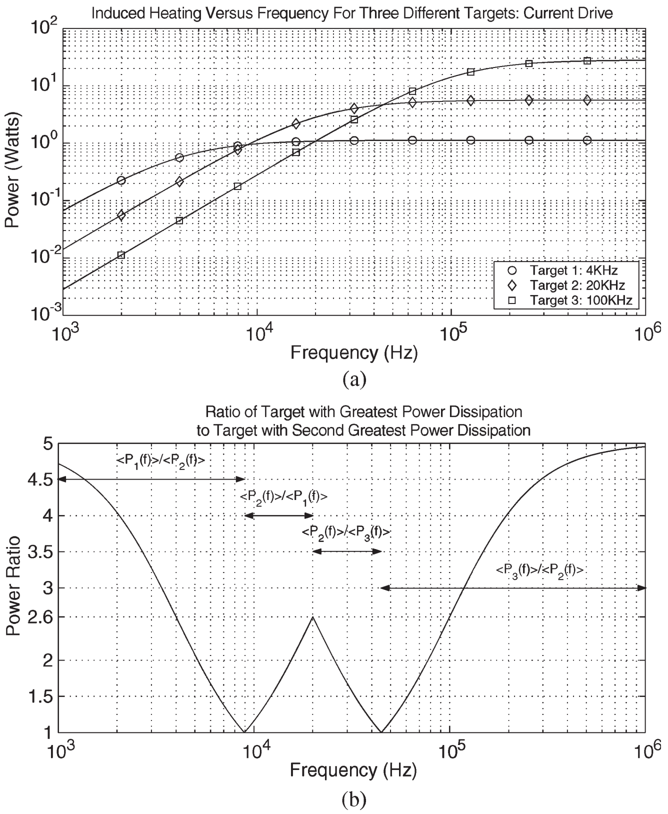

Fig. 6. Induction-heating power curves versus frequency for three different targets, assuming a sinusoidal current-source drive of amplitude $I_o = 1$ A. (a) Power profiles for three different targets. (b) Ratio of the delivered power between targets.

$$I_o(f_{n+1}) = \frac{1}{\sqrt{\alpha}}\frac{K_n}{K_{n+1}} I_o(f_n). \tag{8}$$

B. Experimental Setup: Thin-Walled Cylindrical Shells

To test these models, three thin-walled shells, each measuring $1.25''$ in diameter and $1.00''$ in length, were constructed

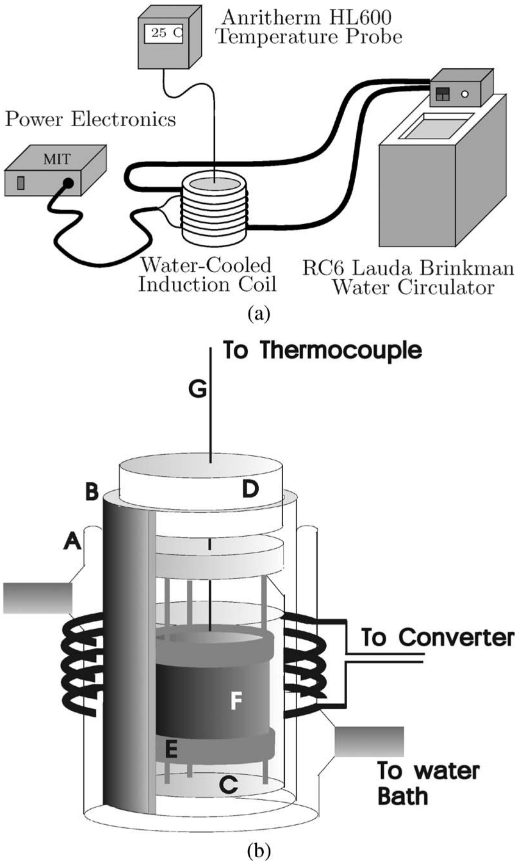

(a)

(b)

Fig. 7. Diagram of the calorimetry test setup. (a) Overall test apparatus. (b) Close-up of the test vessel.

by soldering or brazing together a single piece of 110 annealed copper, alloy 260 brass, or 302 stainless-steel shim, respectively. These dimensions lead to a self-inductance of about 25 nH for each target. In order to achieve a desired separation in resistance of $\alpha \approx 5$, these conductors were chosen with the following respective thicknesses (Δ): 3, 2, and 4 mil. These values result in nominal break-point frequencies of 5.6, 30.2, and 169.2 kHz, respectively. The power dissipation as a function of frequency for each target was determined via a careful calorimetry experiment and was then tabulated.

Fig. 7(a) shows the overall setup for the calorimetry experiment, while Fig. 7(b) shows a close-up of the test vessel. The test is carried out using an induction coil that has been wrapped around a water-cooled glass former (A) that is maintained at a constant 25.0 °C by a Lauda/Brinkman water circulator. This is done to ensure that none of the power dissipated in the induction coil influences the heating of the induction target (F). The induction target is designed to fit onto an acrylic former (E) that, in turn, sits in a water-filled test jar (C). This arrangement ensures that the position of the target with respect to the primary coil is fixed, thereby maintaining a constant coupling coefficient from target to target. A thermocouple probe (G) fits through a small hole in the top of the test jar and is used to measure the temperature of the heated water. To minimize heat transfer between the test jar and the external surroundings, a thick layer of insulating material (B) separates the side walls and bottom of the test jar from the water-cooled glass former, while a styrofoam cap (D) covers the top of the jar.

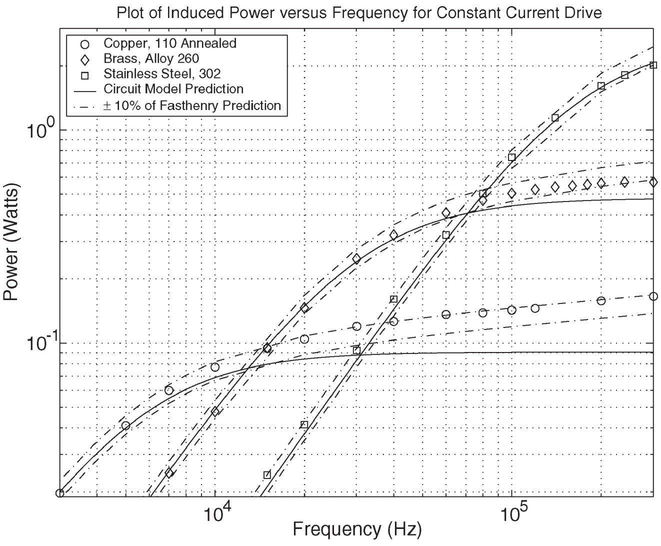

Fig. 8. Calorimetry results for three different induction-heating targets.

The induction coil is driven by a multilevel sine-wave approximation similar to the one shown in Fig. 3(a), and the frequency of the sine wave is varied from 3 to 300 kHz. In order to keep the amplitude of the primary current constant, the voltage amplitude is manually controlled at each frequency. At the desired frequency, a fixed quantity of water (165.2 g) is heated for exactly 1 h starting from the moment it reaches 25.0 °C. At the end of this period, the container is shaken to equalize the internal temperature, and the final temperature is measured by a digital thermometer and is recorded. Although, in principle, the power delivered could be estimated based on the change in temperature by using the mass and specific heat of the water, acrylic former, and glass walls, this method would only be accurate if no energy is lost to the external environment. A better way of calibrating the power delivered from the change in temperature is to run the experiment using a well-defined source of power for exactly 1 h. This was done by dissipating a fixed amount of power in a resistor immersed in the water during separate tests.

C. Results: Thin-Walled Cylindrical Shells

Fig. 8 shows the results of the calorimetry experiment for the three test metals. The simple RL model accurately predicts the power dissipation of the stainless steel and brass conductors over a wide range of frequencies. In the case of the copper target, there is a noticeable discrepancy, particularly at high frequencies. This discrepancy is attributable to the fact that the skin depth is approaching the conductor thickness (at $f =$ 300 kHz and $\delta_{\mathrm{cu}} \approx 1.6\Delta_{\mathrm{cu}}$). As an additional check, a 3-D model of the induction coil and target shown in Fig. 9 was evaluated using the 3-D field solver FastHenry [24] in order to model the skin effect on the ac impedance of each target. The dashed lines in Fig. 8 represent a variation in the FastHenry prediction of $\pm 10\%$ and, as shown, almost completely bound all of the calorimetry data. Variation in the calorimetry data can be attributed to $\pm 10\%$ manufacturing tolerances in the shim thickness, as well as measurement error and unmodeled

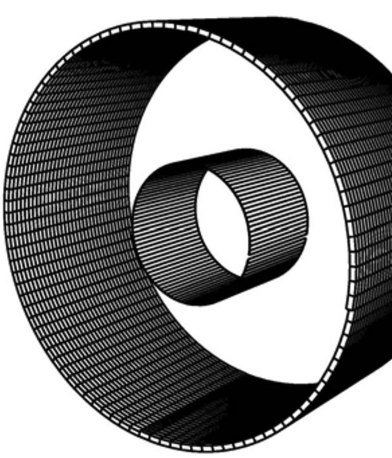

Fig. 9. Three-dimensional model of the primary induction coil and an induction target as used in the calorimetry experiment.

parasitics, such as contact resistance from soldering or brazing each conductor into a cylindrical shell.

D. Induction Heating: Voltage-Drive Case

The current-drive case resulted in easy-to-understand relationships governing the power dissipation in each target. However, the Marx inverter naturally applies a voltage-source drive, not a current one. The analysis of a voltage-driven system is slightly more complicated because the primary current is now a function of the aggregate impedance that the converter must drive. This means that, unlike the current-mode case, the absolute power delivered to a target cannot be analyzed without taking into consideration the effect of all the targets, even if the cross-coupling between targets is negligible. Fortunately, the ratio of power delivered between loads, as shown in Fig. 6, remains unchanged whether a voltage or current drive is employed.

Because of the multiple-output nature of this system, the voltage-mode case can be conveniently described using the following state-space description:

$$[\dot{I}] = [-L^{-1}R][I] + [L^{-1}]\begin{bmatrix} V_{\text{in}} \\ 0 \end{bmatrix} \tag{9}$$

where V_{in} is the amplitude of the input voltage and L is the general inductance matrix of the system, which, for the three-target case, takes the following form:

$$L = \begin{vmatrix} L_0 & L_{01} & L_{02} & L_{03} \\ L_{10} & L_1 & L_{12} & L_{13} \\ L_{20} & L_{21} & L_2 & L_{23} \\ L_{30} & L_{31} & L_{32} & L_3 \end{vmatrix}. \tag{10}$$

Likewise, the resistance matrix R for the primary coil and the three induction targets ($n = 1$, 2, and 3) is

$$R = \begin{vmatrix} R_0 & 0 & 0 & 0 \\ 0 & R_1 & 0 & 0 \\ 0 & 0 & R_2 & 0 \\ 0 & 0 & 0 & R_3 \end{vmatrix}. \tag{11}$$

Using (9), the transfer function from V_{in} to I_n, where I_n denotes the current in conductor n, for the hypothetical system shown in Fig. 6, was calculated in Matlab and is shown in Fig. 10(a). Because the induction coil's impedance grows with frequency (ignoring the effect of parasitic capacitance), the current in each load must drop off at high frequencies. This results in the dissipated power curves for each load shown in Fig. 10(b), where, unlike the current-mode case, power decreases with increasing frequency. Note that power also rolls off at low frequencies because of the finite resistance from the primary coil. In the low-frequency limit, the current through the induction coil approaches a constant value; hence, for low frequencies, the system behavior resembles that of the current-mode case. If the effective resistance of a target is known and does not vary significantly with frequency, the induction-heating profile for that target can be inferred from its V_{in}-to-I_n transfer function. For a sinusoidal voltage drive of amplitude V_{in}, the current (I_n) flowing in conductor n can be determined and used to calculate the power dissipated according to the relationship

$$\langle P_n(\omega)\rangle = \frac{1}{2} I_n(\omega)^2 R_n. \tag{12}$$

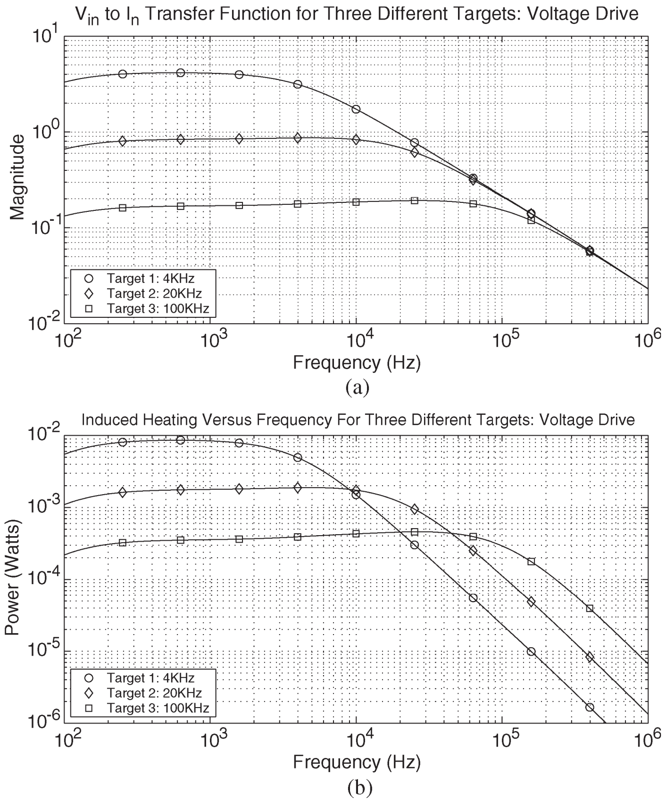

Fig. 10. V_{in}-to-I_n transfer function and power curves versus frequency for three different targets, assuming a sinusoidal voltage drive of amplitude $V_o = 1$ V. (a) Transfer function for three different targets. (b) Power profiles for three different targets.

E. Experimental Setup: Thin-Wire Loops

As a final experiment, a multitarget system was built using three different metal wires: copper, alloy 90, and alloy 800.[1]

---

[1] Alloy 90 and alloy 800 are commercially available resistance wires.

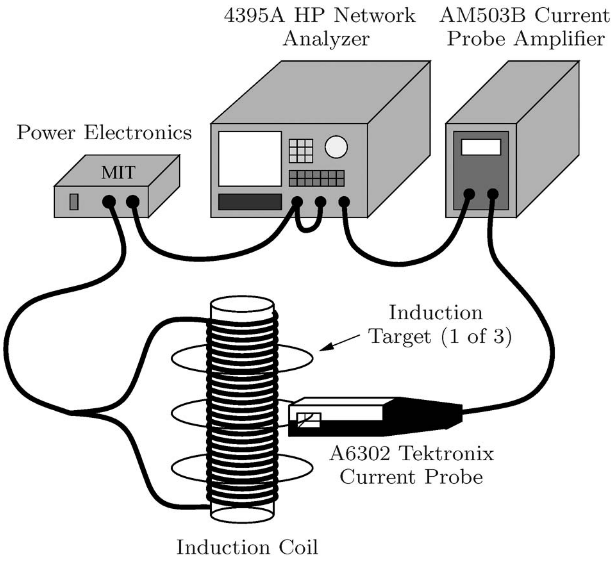

Fig. 11. Nonresonant multiwire induction-heating experiment.

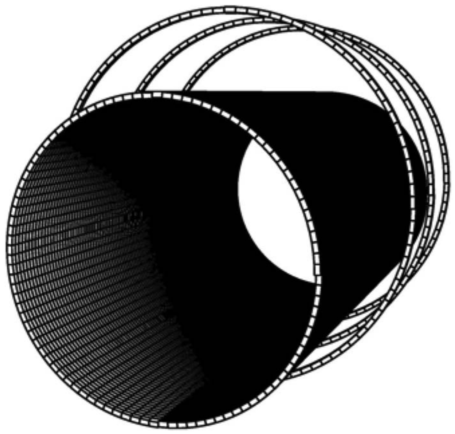

Fig. 12. Three-dimensional model of the primary induction coil and targets as used in the multiwire induction-heating experiment.

For this experiment, each wire had a diameter of 0.08118 cm (20 AWG) and was formed into a loop measuring 6.00 cm in diameter. Each resulting target had a self-inductance of 0.167 μH. The resistances of these alloys are roughly factors of eight to nine apart and were chosen to yield nominal break-point frequencies of 5.98, 51.9, and 461.6 kHz, respectively. The purpose of this experiment was not to measure power directly but to characterize the V_{in}-to-I_n transfer function for all of the targets so that power could be inferred later. Fig. 11 shows the entire system. In this setup, all three wire loops are arranged on a PVC former (not shown) and coupled to a 205-μH induction coil. The center of each target and the induction coil are offset in order to accommodate a A6302 Tektronix current probe. An HP 4395A network analyzer determines the transfer function by sweeping the voltage reference that generates the multilevel sine-wave approximation impressed across the induction coil. The current in each target is then measured via the current probe and amplified before being passed back to the network analyzer.

In order to calculate the theoretical transfer functions for this system, a 3-D model of this system was generated and passed to FastHenry to estimate the inductance matrix for the system. A view of the model used is shown in Fig. 12. In principle, the mutual inductances could have been estimated in a variety of ways, including direct evaluation of the Neumann formula or with a numerical approach such as a mesh-matrix technique [25].

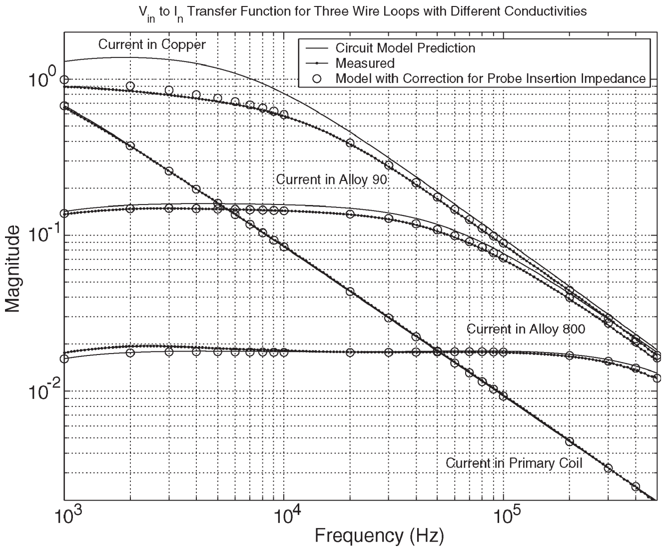

Fig. 13. Results of the multiwire induction-heating experiment.

F. Results: Thin-Wire Loops

The experimental magnitude response of the system is shown in Fig. 13. A discrepancy between the circuit model and the measured data was apparent for the lower resistance wires, particularly the copper wire. This discrepancy is the result of the additional insertion loss added to the wire target by the current probe during the measurement. Because the resistance of the copper wire ($R_{\text{cu}} = 6.28\ \text{m}\Omega$) is comparable to the insertion loss associated with the current probe, it cannot be ignored. This effect is less noticeable for the remaining alloys because of their lower conductivities. To account for this measurement error, the insertion impedance of the probe was characterized over the frequency range in question and then used to calculate what the new magnitude response would be. After allowing for this correction, the measurements agree within about $\pm 10\%$ over the majority of the frequency range. For about 5 kHz and higher, the agreement is closer to $\pm 5\%$. The increased error at low frequencies is due to the unmodeled dynamics from the multilevel inverter as the output capacitors of this stage begin to have some effect.

IV. RESONANT FREQUENCY-SELECTABLE INDUCTION-HEATING TARGETS

Unlike the nonresonant targets in the previous section, the design of a multiple resonant induction target system can be potentially more challenging because of the larger number of parameters to be specified. A designer must simultaneously balance geometry, thermal issues, and the selection of a greater number of components while trying to achieve a desired degree of "selectivity" in an acceptable frequency band. To make matters worse, cross-coupling between targets can create additional resonant and antiresonant frequencies for a target. A designer is

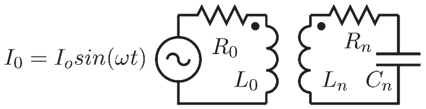

Fig. 14. Induction-heating circuit for one resonant target. In this case, the primary coil is driven by a sinusoidal current.

then forced to evaluate the design using a computer, a method that provides little insight for improvement. Fortunately, some insight can be found by examining cases first that are not highly coupled.

A. Induction Heating: Current-Drive Case

Consider the situation where only one resonant circuit exists ($n = 1$), as shown in Fig. 14 by R_n, L_n, and C_n. This network is coupled to a primary induction coil (L_0), which is driven by the sinusoidal current ($I_0 = I_o \sin(\omega t)$). By denoting the mutual inductance between coils L_0 and L_n as L_{0n}, the coupling coefficient between these two coils (K_n) is then defined as

$$K_n = \frac{L_{0n}}{\sqrt{L_0 L_n}}. \tag{13}$$

The time-averaged power dissipated in R_n can then be expressed as

$$\langle P_n(\omega)\rangle = \frac{(I_o K_n \omega^2)^2 L_0 L_n R_n}{2\left[(1 - L_n C_n \omega^2)^2 + (R_n C_n \omega)^2\right]}. \tag{14}$$

Maximum power is delivered at the natural frequency

$$\omega_n = \frac{1}{\sqrt{L_n C_n}} \tag{15}$$

which simplifies (14) to the following:

$$\langle P_n(\omega_n)\rangle = \frac{(I_o K_n \omega_n)^2 L_0 L_n}{2R_n} = \frac{(I_o K_n)^2 L_0}{2 R_n C_n}. \tag{16}$$

Alternatively, (16) can be expressed in terms of target n's "quality" factor

$$Q_n = \frac{L_n \omega_n}{R_n} \tag{17}$$

to give

$$\langle P_n(Q_n)\rangle = \frac{(I_o Q_n K_n)^2 R_n}{2}. \tag{18}$$

Consequently, the power dissipated in a target is commensurate with its Q. For the current-drive case, these relationships will hold equally well for multiple simultaneous targets, provided that there is no cross-coupling between targets, i.e., any mutual inductance between target coils is identically zero. When at least two targets are present, it is useful to know the frequencies that lead to the greatest amount of preferential heating. The degree of heating in a target n compared to a target m can be expressed as

$$\frac{\langle P_n(\omega)\rangle}{\langle P_m(\omega)\rangle} = \frac{K_n^2 L_n R_n \left[(1 - L_m C_m \omega^2)^2 + (R_m C_m \omega)^2\right]}{K_m^2 L_m R_m \left[(1 - L_n C_n \omega^2)^2 + (R_n C_n \omega)^2\right]}. \tag{19}$$

Taking the derivative of (19) and setting it equal to zero

$$\frac{d}{d\omega}\left(\frac{\langle P_n(\omega)\rangle}{\langle P_m(\omega)\rangle}\right) = 0 \tag{20}$$

leads to a fifth-order polynomial in ω

$$a\omega^5 + b\omega^3 + c\omega = 0 \tag{21}$$

where the coefficients are as follows:

$$\begin{aligned} a &= \left[(R_n C_n)^2 - 2L_n C_n\right](L_m C_m)^2 \\ &\quad - \left[(R_m C_m)^2 - 2L_m C_m\right](L_n C_n)^2 \\ b &= \left[2(L_m C_m)^2 - 2(L_n C_n)^2\right] \\ c &= \left[(R_m C_m)^2 - 2L_m C_m\right] - \left[(R_n C_n)^2 - 2L_n C_n\right]. \end{aligned} \tag{22}$$

Only two of the polynomial's roots are relevant as one of the roots is zero and the other two are negative. The valid roots are

$$\omega = \sqrt{\frac{-b \pm \sqrt{b^2 - 4ac}}{2a}}. \tag{23}$$

If the Q's of the resonant targets are high enough, the solution to (23) will equal the natural frequencies of the two targets to a close approximation. Equation (16) makes apparent that for a fixed current, the absolute power delivered to a target will vary, depending on the target's component values. In order to equalize the absolute power delivered to all targets, the amplitude of the current driving the primary coil can be controlled via the following relationship:

$$I_0(\omega_{n+1}) = \frac{K_n}{K_{n+1}}\sqrt{\frac{R_{n+1} C_{n+1}}{R_n C_n}}\, I_0(\omega_n). \tag{24}$$

These results are easier to understand by examining the time-averaged power versus frequency for the three hypothetical targets shown in Fig. 15(a). In this example, the primary coil $L_0 = 10\ \mu$H, and the inductance of the three ($n = 1, 2, 3$) target coils is $L_n = 100\ \mu$H. Likewise, their resistances are given by $R_n = 1\ \Omega$. The resistance (R_0) of the primary coil is also 1 Ω but is irrelevant because of the current-source drive. The coupling coefficient of all targets has been arbitrarily set to 0.3, and the capacitances (C_n) of the three targets ($n = 1, 2, 3$) have been chosen to give natural frequencies at 80, 90, and 100 kHz. With these constraints, each target experiences preferential heating with respect to the remaining targets over some frequency range. The extent of preferential heating is given as a ratio in Fig. 15(b) and clearly exceeds 100 near the natural frequencies of the targets in this example.

So far, only targets with negligible cross-coupling have been considered. In reality, mutual inductance always exists between targets and cannot always be ignored. Even a small degree of cross-coupling can have a noticeable effect on the power profile of a resonant target. The inclusion of cross-coupling terms leads to increasingly complicated transfer function descriptions of the system without much additional insight. Instead of looking at the transfer functions in detail, consider the impact

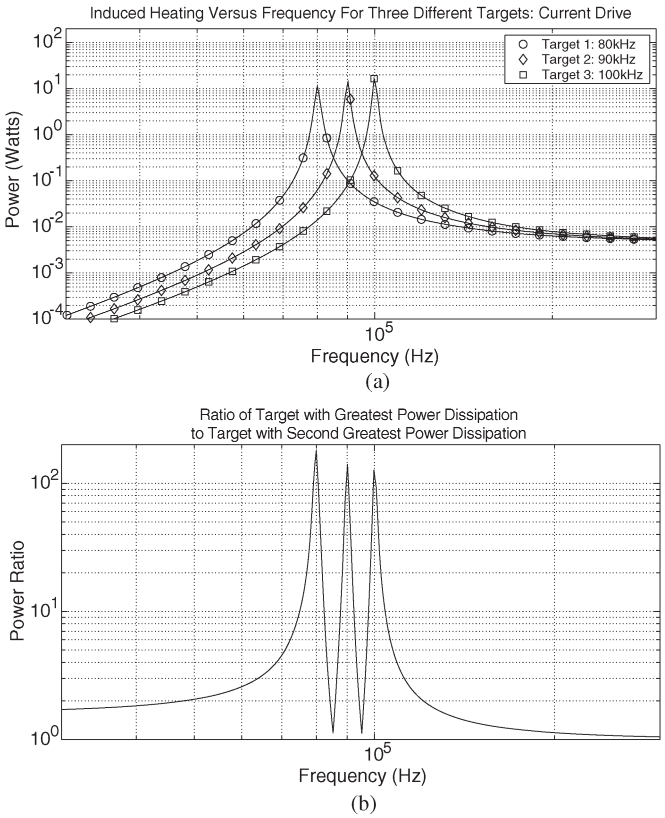

(a)

(b)

Fig. 15. Induction-heating power curves versus frequency for three different targets, assuming a sinusoidal current-source drive of amplitude $I_o = 1$ A. (a) Power profiles for three different targets. (b) Ratio of the delivered power between targets.

of cross-coupling on the hypothetical targets discussed earlier. For simplicity, target 3 has been removed, and targets 1 and 2 now have a cross-coupling coefficient of 0.03, a number which is ten times smaller than their respective coupling to the primary coil. For this example, the power profiles of the two targets are shown in Fig. 16(a). Previously, each target exhibited one resonant frequency. Now, each target experiences an additional resonance located close to the natural frequency of the target that it is cross-coupled to, as well as an antiresonance to the right of this "new resonant frequency." Fig. 16(b) shows the ratio of heating between targets. From this figure, it is apparent that the frequencies where the ratio is maximized are now higher, corresponding more closely to the location of the antiresonant frequencies.

B. Induction Heating: Voltage-Drive Case

The current-drive case is insightful because it makes apparent the excitation frequencies that give the greatest degree of preferential heating. The Marx inverter naturally applies a voltage at its output and supplies current, as determined by the driving-point impedance. If the impedance looking into the primary coil is known, the current drawn from the converter can be calculated, and the equations from the previous section can be applied.

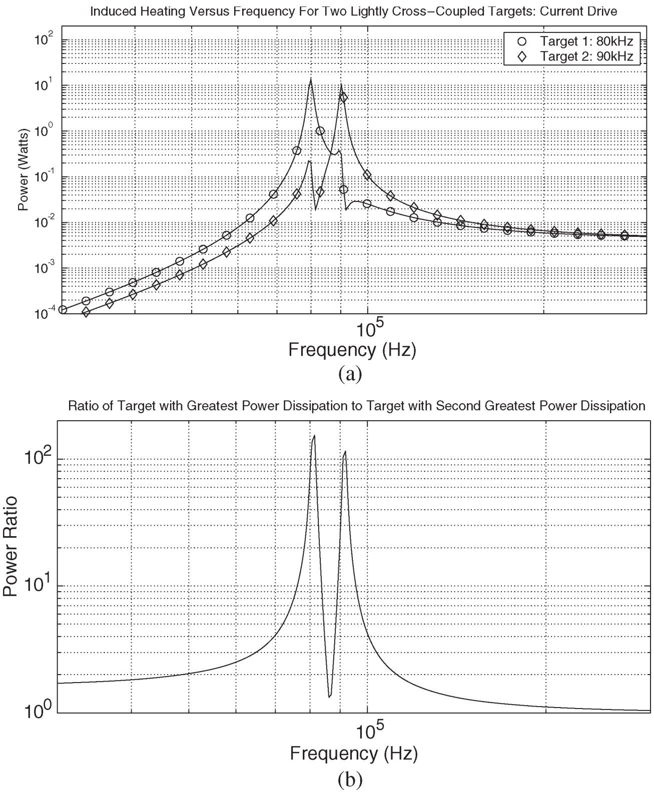

(a)

(b)

Fig. 16. Induction-heating power curves versus frequency for two different targets, assuming a sinusoidal current-source drive of amplitude $I_o = 1$ A. (a) Power profiles for two different targets. (b) Ratio of the delivered power between targets.

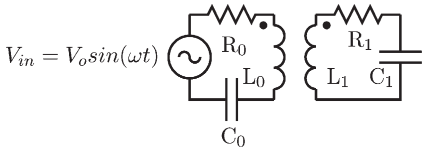

Fig. 17. Induction-heating circuit for one resonant target: Voltage drive.

Consider Fig. 17 that represents the induction-heating circuit from before with some minor changes. The current source has been replaced with a voltage source, and as a practical matter, a dc-blocking capacitor C_0 has been inserted on the source side. If only one target is present, the expression for the load impedance $Z_{\text{load}}(s)$ is a rational transfer function of the form

$$Z_{\text{load}}(s) = \frac{Z_n(s)}{Z_d(s)} \tag{25}$$

where the numerator is

$$Z_n(s) = \left(L_0 s + R_0 + \frac{1}{C_0 s}\right)\left(L_1 s + R_1 + \frac{1}{C_1 s}\right) - (L_{01} s)^2 \tag{26}$$

and the denominator is

$$Z_d(s) = \left(L_1 s + R_1 + \frac{1}{C_1 s}\right). \tag{27}$$

If the impedances associated with R_0 and C_0 are small at the frequencies of interest (typical of a practical design), then (25) can be simplified to

$$Z_{\text{load}}(s) = \frac{L_0 s\left[L_1(1-K_1^2)C_1 s^2 + R_1 C_1 s + 1\right]}{L_1 C_1 s^2 + R_1 C_1 s + 1}. \tag{28}$$

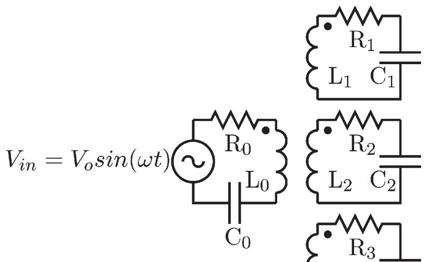

Fig. 18. Induction-heating circuit for three different targets.

From (28), it can be inferred that the load impedance will experience a maximum near the natural frequency of the target

$$\omega_{Z\max} = \omega_1 = \frac{1}{\sqrt{L_1 C_1}} \tag{29}$$

and a minimum near

$$\omega_{Z\min} = \frac{1}{\sqrt{L_1 C_1 \left(1 - K_1^2\right)}}. \tag{30}$$

This suggests that, for multiple resonant targets (with negligible cross-coupling), the load impedance will experience a local maximum at the natural frequencies of each individual target. The frequencies that lead to the greatest preferential heating can therefore be determined by examining where the load impedance experiences a local maximum.

When more than one target is present and the impact of cross-coupled inductors must be taken into account, the system shown in Fig. 18 can be analyzed using the following compact state-space formulation:

$$\begin{bmatrix} \dot{I} \\ \dot{V} \end{bmatrix} = \begin{bmatrix} -L^{-1}R & L^{-1} \\ -C^{-1} & 0 \end{bmatrix} \begin{bmatrix} I \\ V \end{bmatrix} + \begin{bmatrix} L^{-1} & 0 \\ 0 & 0 \end{bmatrix} \begin{bmatrix} V_{\text{in}} \\ 0 \end{bmatrix} \tag{31}$$

where V_{in} is the input voltage and L is the general inductance matrix of the system, which, for the three-target case, takes the following form:

$$L = \begin{vmatrix} L_0 & L_{01} & L_{02} & L_{03} \\ L_{10} & L_1 & L_{12} & L_{13} \\ L_{20} & L_{21} & L_2 & L_{23} \\ L_{30} & L_{31} & L_{32} & L_3 \end{vmatrix}. \tag{32}$$

Likewise, the resistance and capacitance matrices R and C for the three-target network in Fig. 18 can be expressed, respectively, as

$$R = \begin{vmatrix} R_0 & 0 & 0 & 0 \\ 0 & R_1 & 0 & 0 \\ 0 & 0 & R_2 & 0 \\ 0 & 0 & 0 & R_3 \end{vmatrix} \tag{33}$$

$$C = \begin{vmatrix} C_0 & 0 & 0 & 0 \\ 0 & C_1 & 0 & 0 \\ 0 & 0 & C_2 & 0 \\ 0 & 0 & 0 & C_3 \end{vmatrix}. \tag{34}$$

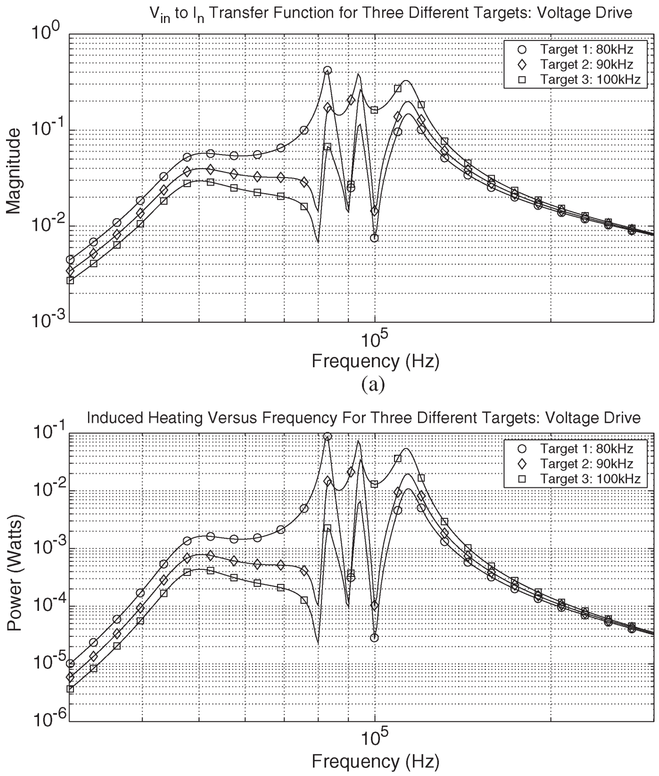

(a)

(b)

Fig. 19. V_{in}-to-I_n transfer function and power curves versus frequency for three different targets, assuming a sinusoidal voltage drive of amplitude $V_o = 1$ V. (a) Transfer function for three different targets. (b) Power profiles for three different targets.

Using (31), the transfer function from V_{in} to I_n (where I_n denotes the current in conductor n for the hypothetical system shown in Fig. 18) was calculated in Matlab and is shown in Fig. 19(a). This example has identical component values to the hypothetical system discussed in the current-drive case (with no cross-coupling). The only difference is the addition of C_0, the dc-blocking capacitor that has been chosen to yield a natural frequency with the primary-side coil of 50 kHz. If the effective resistance of a target is known and does not vary significantly with frequency, the induction-heating profile for that target can be determined from its V_{in}-to-I_n transfer function. For a sinusoidal voltage drive of amplitude V_o, the current flowing in conductor n can be found from Fig. 19(a) and used to calculate the power dissipated according to the relationship

$$\langle P_n(\omega) \rangle = \frac{1}{2} I_n(\omega)^2 R_n. \tag{35}$$

Carrying this calculation out results in the dissipated power curves of each load shown in Fig. 19(b). In this example, the power curves are similar in shape to the magnitude of the transfer function because all of the targets have the same resistance. The voltage-source case results in power profiles that are arguably more complicated than that in the current-source case. Although the frequencies that give the most preferential heating are unchanged from the current-drive case, they no longer maximize the amount of power delivered. As stated previously, this can be explained by the variation of the load impedance as a function of frequency. The magnitude and phase of the load impedance for this example are shown in Fig. 20(a) and (b), respectively. As suggested earlier, the magnitude of the

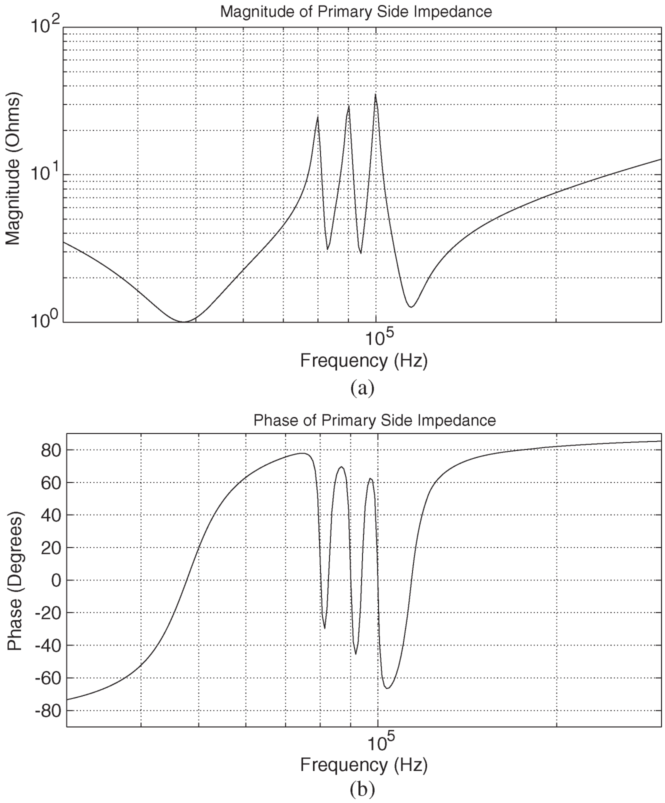

Fig. 20. Load impedance as seen by converter versus frequency. (a) Magnitude of load impedance. (b) Phase of load impedance.

impedance peaks at the frequencies corresponding to the natural frequencies of the various targets. The increased impedance leads to less current drawn and, hence, a reduction in power. At these frequencies, the phase approaches 0°, so the impedance appears resistive here. The phase also passes through 0° at frequencies where the power dissipated in a target is maximized. However, the degree of preferential heating is much smaller there.

C. Practical Issues

Resonant RLC induction targets can be constructed in a number of ways. Perhaps the easiest approach is to design each target using a passive element for each of its constituent components, i.e., a separate resistor, inductor, and capacitor. For the gel damper application, this approach is less than desirable. Using a lumped resistor as the dissipative element localizes heating to a small area while consuming precious volume in the gel chamber. A better approach is to rely on the parasitic resistance of the induction coil. If the coil windings are evenly distributed, a uniform heating surface can be built. The capacitor could also be eliminated if the self-resonance of the coil is low enough. However, if the interwinding capacitance of the coil is insufficient, a lumped capacitor must be carefully selected. Because the selectivity of these targets relies on sufficiently high "Q's," it is not uncommon for the winding resistance to be small and the induced current to be high. From a practical standpoint, the selected capacitor should have an equivalent series resistance that is much smaller than the winding resistance. Otherwise, most of the induced heating will occur in the capacitor and not the windings. This is undesirable because the resonant frequency may change significantly with temperature, and constant cycling can cause the capacitor to fail. Stable capacitors with low dissipation factors, such as silvered mica, are ideal for this application, provided that the appropriate values are available in reasonable volumes.

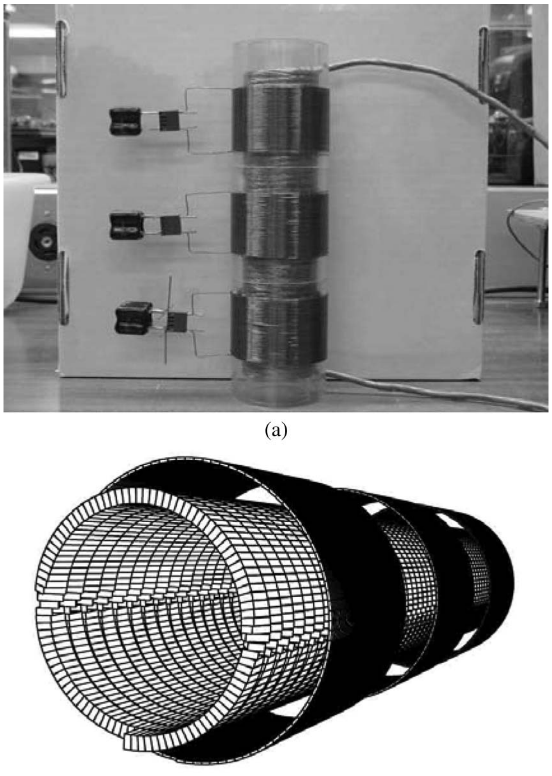
(a)

(b)

Fig. 21. Multiresonant induction-heating system. (a) Photograph of the system. (b) Three-dimensional FastHenry model of the system.

D. Experimental Setup: Resonant Targets

A resonant multitarget system consisting of a primary coil and three target coils was built for testing. A photograph of this system can be seen in Fig. 21(a). The primary coil has a diameter of 4.4 cm and a length of 20.4 cm and was made from 48 turns of litz wire on a plexiglass former. The three resonant targets have the same 6.32-cm diameter with the following lengths: 4.0, 4.1, and 4.2 cm. These coils were made from 57, 58, and 59 turns of 22-AWG wire, respectively. The outputs of these targets were paralleled using silvered-mica capacitors of the following values: 30, 20, and 40 nF. The self-inductances of these coils along with the mentioned capacitor values give natural frequencies of 56.1, 67.2, and 81.9 kHz, as determined by (15).

In order to calculate the theoretical transfer functions of the system, a 3-D model of each coil was generated and passed to FastHenry [24] to estimate the inductance matrix for the system. A view of the model used is shown in Fig. 21(b). The actual transfer functions were then measured for comparison using the test setup shown in Fig. 22. An HP 4395A network

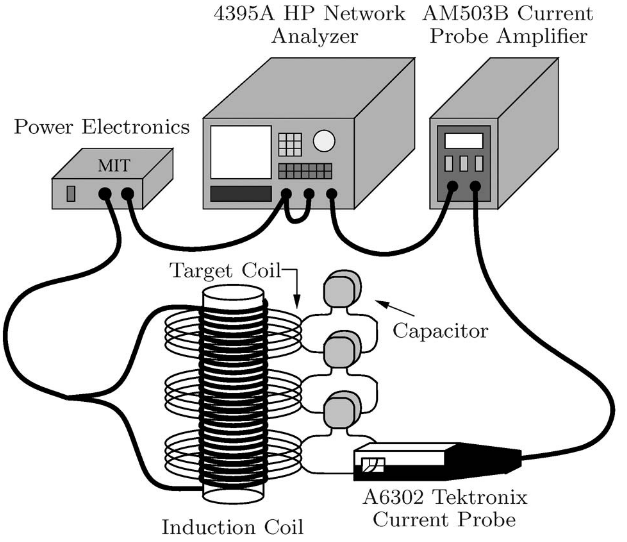

Fig. 22. Multiresonant induction-heating experiment.

analyzer determined the transfer function by sweeping the voltage reference that generates the multilevel sine-wave approximation impressed across the induction coil. The current in each target is then measured via the current probe and amplified before being passed back to the network analyzer. Once all of the $V_{\rm in}$-to-I_n transfer functions have been characterized, the power profile of each target can be estimated using (35), as discussed previously.

E. Results: Resonant Targets

The measured results from the network analyzer are shown against a theoretical prediction in Fig. 23. It is clear from the figure that most of the salient features are in agreement. Notably, the locations of all resonances and antiresonances are within a few percent of their predicted locations. Even the highest frequency peaks agree within about 3%. In general, the magnitudes of the measured resonances and antiresonances agree at low frequencies. However, there is a growing error with increasing frequency. The reason for this discrepancy can be attributed to the additional ac losses in the windings as a result of skin and proximity effects at higher frequencies. These losses cause the measured maxima and minima to appear more damped than predicted. For this particular fit, the ac resistances of the windings were measured at low-frequency resonances and used to estimate the transfer functions. When this resistance is measured for a higher frequency resonance, the fit improves on the high end. Consequently, if the ac resistance could be characterized across frequencies, the overall fit could be improved as well [22].

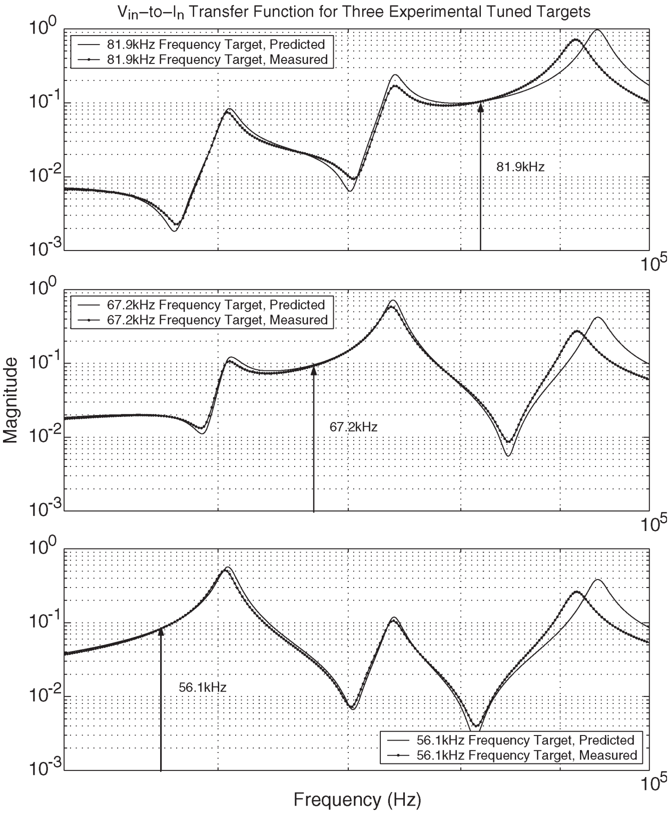

Fig. 23. $V_{\rm in}$-to-I_{in} transfer function results of the multiresonant induction-heating experiment.

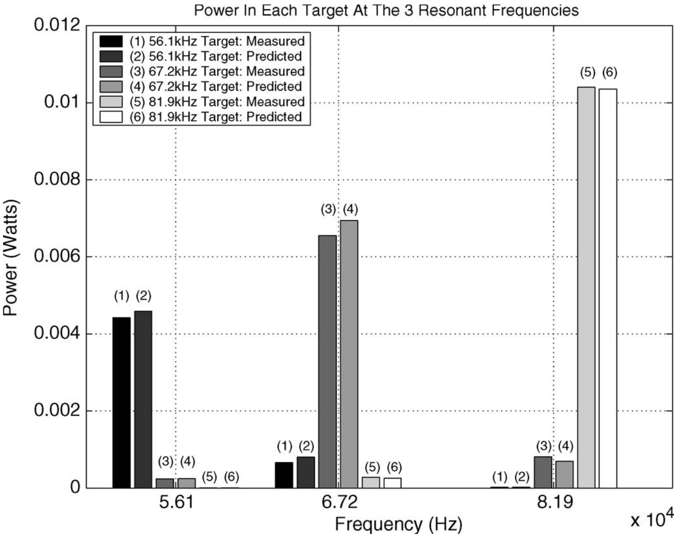

Fig. 24. Dissipated power in each of the three targets when driven at their respective resonant frequencies by a sinusoidal voltage drive of amplitude $V_o = 1$ V. Both calculated and measured results are shown.

Ultimately, a designer is concerned with the actual power dissipated by a given target and not the current induced in it. The delivered power can be determined using measurements of each target's ac resistance for the three resonant frequencies of operation. If these measured resistances are used to populate the terms in (33), then (31) can be solved at each resonant frequency. Finally, the power dissipated by a target at each resonant frequency can be calculated using (35). The results of both measured and predicted transfer functions are shown in Fig. 24 for the current example. Clearly, the measured and predicted power dissipations in each resonant target agree closely. Of the three targets, the middle one (56.1 kHz) is the least accurate but is still within about 6%.

V. CHOOSING BETWEEN NONRESONANT AND RESONANT TARGETS

When deciding between nonresonant and resonant induction targets for an application, a designer should keep in mind a number of important criteria. Nonresonant-target topologies using thin-walled conductors are generally easier to construct than RLC-type resonant targets. In addition, they are more durable and less likely to exhibit variations in frequency response with temperature. Despite these advantages, the degree of frequency selectivity that can be achieved with thin-walled conductors is modest, which is directly proportional to α. As the number of α-spaced targets increases, the demand on the excitation source's dynamic frequency range quickly becomes untenable, growing at a rate of α^{n-1}.

By contrast, resonant targets offer high selectivity and lend themselves to applications that require large numbers of individual targets. This selectivity comes at a price, however. As mentioned earlier, the capacitors chosen for these targets should have high Q's to prevent unnecessary heating in the capacitor itself. Variations in capacitance due to temperature fluctuations will also lead to drift in a target's resonant frequency. If this drift is sufficiently high, active tracking of the resonant frequency may be required. Additional considerations for resonant targets also include the need for wiring insulation in the resonant coil suitable for the application's temperature requirements. Last, capacitors may preclude certain applications, i.e., those involving environments with high humidity.

The prototype DVA discussed initially in Section I made use of thin-walled cylindrical shells similar in construction to the ones described in Section III. It was decided that resonant targets were not well suited to this application because the necessary capacitor would have to be suspended in the gel solvent. While, in theory, the capacitor could be placed outside of the compartment, this would result in increased manufacturing complexity because the capacitor terminals would have to penetrate the compartment wall while maintaining a water-tight seal. Finally, of the two nonresonant topologies considered in this paper, the cylindrical shell's provide an increased surface area for heat delivery when compared to thin-wire loops.

VI. CONCLUSION

The frequency-selectable induction-heating targets considered in this paper are classified as either nonresonant or resonant targets. It was shown that nonresonant targets can be constructed using single-turn conductors whose critical dimensions are small compared to their skin depth(s) at the frequency range of interest. When these single-turn conductors have similar self-inductances and R/L break-point frequencies that are spaced evenly by factors of α, frequency selectivity is achieved. That is to say, a target driven at its break-point frequency heats by at least an amount $(\alpha^2 + 1)/(2\alpha)$ more than the remaining targets. These results were experimentally demonstrated for two types of induction targets, namely, thin-walled cylindrical shells and thin-wire loops. Resonant targets were also considered and later constructed using RLC circuits. It was seen that by designing each target coil and capacitor to have a different resonant frequency, frequency selectivity could also be achieved. An experimental system consisting of three resonant targets was built and tested.

One application of these targets is a tunable vibration damper that is being developed. This damper relies on the fact that a rotating container filled with a variable viscosity material can alter its moment of inertia. In this case, the rotating container consists of a set of individual compartments filled with a thermally responsive gel polymer. Thermal stimulation of the different compartments allows the damper to adjust the location of its antiresonant frequency. One way to thermally activate these compartments is by outfitting each chamber with a frequency-selectable induction target. Any combination of chambers can then be simultaneously heated by the primary induction coil if it is driven at the appropriate frequencies with a voltage sum of sine waves.

REFERENCES

[1] C. Harris and C. Crede, *Shock and Vibration Handbook*, vol. 1. New York: McGraw-Hill, 1961.

[2] C. Ting-Kong, *Design of an Adaptive Dynamic Vibration Absorber*. Adelaide, Australia: Dept. Mech. Eng., Univ. Adelaide, Apr. 1999.

[3] T. Tanaka, "Gels," *Sci. Amer.*, vol. 244, no. 1, pp. 124–138, Jan. 1981.

[4] J. Acero, J. M. Burdio, L. A. Barragan, D. Navarro, R. Alonso, J. R. Garcia, F. Monterde, P. Hernandez, S. Llorente, and I. Garde, "The domestic induction heating appliance: An overview of recent research," in *Proc. IEEE Appl. Power Electron. Conf.*, Feb. 2008, pp. 651–657.

[5] V. Esteve, J. Jordan, E. J. Dede, E. Sanchis-Kilders, and E. Maset, "Induction heating inverter with simultaneous dual-frequency output," in *Proc. IEEE Appl. Power Electron. Conf.*, Mar. 2006, pp. 1505–1509.

[6] D. K. Jackson, S. B. Leeb, A. H. Mitwalli, P. Narvaez, D. Fusco, and E. C. Lupton, Jr., "Power electronic drives for magnetically triggered gels," *IEEE Trans. Ind. Electron.*, vol. 44, no. 2, pp. 217–225, Apr. 1997.

[7] A. Boadi, Y. Tsuchida, T. Todaka, and M. Enokizono, "Designing of suitable construction of high-frequency induction heating coil by using finite-element method," *IEEE Trans. Magn.*, vol. 41, no. 10, pp. 4048–4050, Oct. 2005.

[8] D. Puyal, C. Bernal, J. M. Burdio, I. Millan, and J. Acero, "A new dynamic electrical model of domestic induction heating loads," in *Proc. IEEE Appl. Power Electron. Conf.*, Feb. 2008, pp. 409–414.

[9] O. Lucia, J. M. Burdio, I. Millan, J. Acero, and D. Puyal, "Load-adaptive control algorithm of half-bridge series resonant inverter for domestic induction heating," *IEEE Trans. Ind. Electron.*, vol. 56, no. 8, pp. 3106–3116, Aug. 2009.

[10] F. Forest, S. Faucher, J.-Y. Gaspard, D. Montloup, J.-J. Huselstein, and C. Joubert, "Frequency-synchronized resonant converters for the supply of multiwinding coils in induction cooking appliances," *IEEE Trans. Ind. Electron.*, vol. 54, no. 1, pp. 441–452, Feb. 2007.

[11] H. Fujita, N. Uchida, and K. Ozaki, "Zone-controlled induction heating (ZCIH)—A new concept in induction heating," in *Proc. Power Convers. Conf.*, Apr. 2007, pp. 1498–1504.

[12] Y. C. Jung, "Dual half bridge series resonant inverter for induction heating appliance with two loads," *Electron. Lett.*, vol. 35, no. 16, pp. 1345–1346, Aug. 1999.

[13] F. Forest, E. Laboure, F. Costa, and J. Y. Gaspard, "Principle of a multi-load/single converter system for low power induction heating," *IEEE Trans. Power Electron.*, vol. 15, no. 2, pp. 223–230, Mar. 2000.

[14] D. S. Schatz and J. M. Dorrenbacher, "Frequency selected, variable output inductor heater system," U.S. Patent 6 316 754 B1, Nov. 13, 2001.

[15] J. Rodriguez, J. Lai, and F. Peng, "Multilevel inverters: A survey of topologies, controls, and applications," *IEEE Trans. Ind. Electron.*, vol. 49, no. 4, pp. 724–738, Aug. 2002.

[16] S. Daher, J. Schmid, and F. L. M. Antunes, "Multilevel inverter topologies for stand-alone PV systems," *IEEE Trans. Ind. Electron.*, vol. 55, no. 7, pp. 2703–2712, Jul. 2008.

[17] G. P. Adam, S. J. Finney, A. M. Massoud, and B. W. Williams, "Capacitor balance issues of the diode-clamped multilevel inverter operated in a quasi two-state mode," *IEEE Trans. Ind. Electron.*, vol. 55, no. 8, pp. 3088–3099, Aug. 2008.

[18] B. Diong, S. Basireddy, K. Corzine, and Y. Familiant, "Multilevel inverters with equal or unequal sources for dual-frequency induction heating," in *Proc. IEEE Appl. Power Electron. Conf.*, Feb. 2004, pp. 825–831.

[19] J. I. Rodriguez and S. B. Leeb, "A multilevel inverter topology for inductively coupled power transfer," *IEEE Trans. Power Electron.*, vol. 21, no. 6, pp. 1607–1617, Nov. 2006.

[20] J. I. Rodriguez, R. He, and S. Leeb, "Frequency selectable induction heating targets," in *Proc. IEEE Power Electron. Spec. Conf.*, Jun. 2003, pp. 1943–1950.

[21] J. I. Rodriguez and S. Leeb, "Resonant frequency selectable induction heating targets," in *Proc. IEEE Appl. Power Electron. Conf.*, Feb. 2004, pp. 1877–1883.

[22] J. I. Rodriguez, "A multi-frequency induction heating system for a thermally triggered gel polymer dynamic vibration absorber," Ph.D. dissertation, Massachusetts Inst. Technol., Cambridge, MA, Sep. 2003.

[23] H. A. Haus and J. R. Melcher, *Electromagnetic Fields and Energy*. Englewood Cliffs, NJ: Prentice-Hall, 1989, pp. 446–447.

[24] M. Kamon, M. J. Ttsuk, and J. K. White, "FASTHENRY: A multipole-accelerated 3-D inductance extraction program," *IEEE Trans. Microw. Theory Tech.*, vol. 42, no. 9, pp. 1750–1758, Sep. 1994.

[25] K. Kim, E. Levi, Z. Zabar, and L. Birenbaum, "Mutual inductance of noncoaxial circular coils with constant current density," *IEEE Trans. Magn.*, vol. 33, no. 5, pp. 4303–4309, Sep. 1997.

John I. Rodriguez (S'02–M'04) received the B.S., M.Eng., and Ph.D. degrees in electrical engineering from the Massachusetts Institute of Technology (MIT), Cambridge, in 1997, 1999, and 2003, respectively. While working toward the Ph.D. degree, he was a Research Assistant in the Laboratory for Electromagnetic and Electronic Systems, MIT.

He was formerly a Senior Scientist with NEMOmetrics Corporation, Brighton, MA. His research interests include power electronics, multilevel power conversion, induction heating, analog circuit design, and classical feedback control systems.

Steven B. Leeb (S'89–M'93–SM'01–F'07) received B.S., M.S., E.E., and Ph.D. degrees from the Massachusetts Institute of Technology (MIT), Cambridge.

He has been a Member of the Faculty in the Department of Electrical Engineering and Computer Science, MIT, since 1993, where he is currently a MacVicar Faculty Fellow and Professor of electrical engineering and computer science in the Laboratory for Electromagnetic and Electronic Systems and also holds a joint appointment in the Department of Mechanical Engineering. He is concerned with the design, analysis, development, and maintenance process for all kinds of machinery with electrical actuators, sensors, or power-electronic drives.